Investigation of the Critical Factors Controlling Sheared Edge Stretching of Ultra-High Strength Dual-Phase Steels

Yingjie Wu[1], Juha Uusitalo[2] and Anthony J. DeArdo[1,2]*

[1] Basic Metals Processing Research Institute, Department of Mechanical Engineering and Materials Science, Swanson School of Engineering, University of Pittsburgh, Pittsburgh, PA 15261, USA.

[2] Centre for Advanced Steels Research, Materials Engineering Laboratory, Department of Mechanical Engineering, University of Oulu, Oulu, FI-90014, Finland.

ORCID numbers of all authors and the email address of the corresponding author:

Y. Wu: 0000-0002-7062-7568

J. Uusitalo: 0000-0001-7393-6465

A. J. DeArdo*: 0000-0003-3485-4496; deardo@pitt.edu (Corresponding co-author).

Abstract

The present study aimed to explore dual-phase (DP) steels with a good combination of high strength and reasonable global ductility (i.e., total elongation and general stretch formability) and local ductility (i.e., sheared edge ductility or hole expansion ratio). Therefore, a series of ultra-high strength dual-phase steels were designed, melted, rolled, annealed and formed. These steels contained various aluminum additions and vanadium contents and were processed with different coiling temperatures and continuous galvanizing line (CGL) thermal path simulations conducted using a Gleeble 3800 system. The microstructures, tensile properties and hole expansion behaviors of all candidate DP steels were determined and compared. The microstructural and damage evolutions in the process of both hole punching and hole expansion were examined. The results indicated that hole expansion ratios of DP steels could be correlated well with (i) the burnished-to-fracture zone ratios in shear surfaces after hole punching, (ii) the values of reduction in area of tensile specimens after fracturing, and (iii) nanohardness difference between soft ferrite and hard constituents. The micro-voids and micro-cracks introduced by hole punching acted as crack initiation sites, which severely affected the subsequent hole expansion process. Therefore, better

sheared edge ductility may benefit from microstructures that retard the crack propagation or void growth and coalescence during hole expansion.

Keywords: Dual-Phase Steels, Continuous Galvanizing Lines, Hole Expansion, Hole Punching, Shear Surface, Reduction in Area, Fracture Mechanism, Nanoindentation

1. Introduction

Dual-phase (DP) steels are a good representative of advanced high strength steels (AHSS), which are widely applied as automotive structural materials [1]. Since the use of these steels can help improve the safety of vehicles by increasing fracture resistance, as well as increasing the necessary deformation energy required for failure, which leads to an increase in a vehicle's power to weight ratio, thus lowering overall emissions and simultaneously increasing gas mileage. At room temperature, DP steels are characterized by a mixture of ferrite and martensite with/without a third phase, i.e., pearlite [2], bainite [3] or tempered martensite [4,5] due to changes in compositions or processing. The existence of dual-phase structures enables DP steels to obtain low yield strength (YS), high ultimate tensile strength (UTS), high initial strain hardening ratio (n) and reasonable global ductility (i.e., uniform elongation (UE) and total elongation (TE)) [4–8].

In addition to global ductility, local ductility (i.e., sheared edge ductility) of DP steels also needs to reach the requirements of automotive applications. Normally, the hole expansion ratio (HER) is a good indicator of evaluating sheared edge ductility of sheet materials [9]. Many researchers have attempted to correlate tensile properties, i.e., YS [10], UTS [10,11], yield to tensile strength ratio (YS/UTS) [12], post uniform elongation (Post UE) [10,11,13], and normal anisotropy ($\overline{\mathrm{R}}$) [10,14] with HER. However, these universal trends are only valid for single-phase steels and mild steels but are of limited use for complex-phase steels or advanced high strength steels. The effects of microstructural characteristics, i.e., grain size [15], martensite island size [11], martensite volume fraction [9,16], martensite morphology [11], and the amount of retained austenite [17,18] on HER have also been investigated in the literature. Transformation induced plasticity (TRIP)-assisted DP steels are expected to have a better sheared edge ductility due to the existence of retained austenite which can transform into fresh martensite during hole expansion [19]. Additionally, the stable lath retained austenite can relax the stress or strain concentration caused by plastic deformation or phase transformation and hence retard the propagation of micro-cracks or growth of micro-voids during hole expansion [20,21]. Aluminum is often used in TRIP or TRIP-assisted steels, since it can suppress the formation of cementite, resulting in carbon enrichment and stability of remained austenite after the bainitic transformation [22]

Hasegawa et al. [23] reported that hole expansion behaviors of high strength DP steels can be improved by decreasing the hardness difference between soft ferrite and fresh martensite, although the hardness of each constituent was calculated by empirical formula. Later, Taylor et al. applied nanoindentation technology to determine of the nanohardness values of ferrite and hard constituents of DP 980 steels. They found that reducing hardness in both ferrite and hard constituents results in an increase in HER values, but with the loss of UTS. So, it is important to investigate key factors improving hole expansion behaviors of high strength DP steels without a large sacrifice of UTS.

From the literature [24–27], HER values are dependent on the approaches used in hole formation and further processing and emphasized the significance of micro-voids or micro-cracks introduced by hole forming. Hole punching at room temperature is the most cost-effective way of forming a hole, compared with other methods. So, it is necessary to have a deeper understanding of the punching process and its effect on subsequent hole expansion behaviors. Punching is a shearing process which separates hole expansion specimens into two parts and generates initial hole surfaces in the remaining blank along with shear-affected zones (SAZ) with sheared edges [28]. Micro-cracks or micro-voids are often observed relevant to martensite cracking, debonding of ferrite/martensite interfaces, the presence of inclusion particles (i.e., MnS) and decohesion of ferrite/ferrite grain boundaries [23,27,29]. Also, in Wu et al.'s research [5], it was found that internal plastic strains caused by hole punching have a high degree of strain localization at the initial hole-edge region. This results in a deformation gradient where the strain decreases with increasing distance from the sheared edge. This shearing damage was observed to influence the subsequent hole expansion process.

Also, Kahziz et al [30] used 3D synchrotron laminographic technology to observe and interpret damage evolution (i.e., ductile fracture) of sheared edges of DP 600 steels before and after crack mouth opening displacement (CMOD), which stimulated hole expansion tests. However, there is doubt that the deformation and fracture of a specimen with one sheared edge is analogous to those of flat sheet after punching and hole expansion. Also, the deformation conditions for those DP steels with single crack edges studied by Kahziz et al. are not realistic deformation condition for high-strength DP steels. Realistic hole punching deformation means bending followed by balanced biaxial tension. However, Yoon et al [31] reported that fracture toughness may exhibit a good correlation with sheared edge ductility of DP steels. One major problem why the HER test cannot be considered as a true fracture toughness test is because valid fracture toughness tests are to be conducted according to ASTM E1820 [32], which requires the specimen thickness to be large enough for valid plane strain conditions. In this case the observed K_{IC} can be considered a material property, and the fracture in the HER test might indeed be governed by fracture toughness. However, in a thin sheet, such as used in the current experiments, the stress state is plane stress, and, therefore, the observed K_{IQ} is neither a material property nor even known with reasonable accuracy. Since, in the need of automotive lightening, the thickness of typical cold rolled and annealed DP steels ranges from 1.0 mm to 1.5 mm, the use of fracture toughness is questionable.

The present study has investigated candidate DP steels with different pre-annealing conditions (i.e., aluminum levels, vanadium contents and coiling temperatures) and CGL simulations conducted using a Gleeble 3800 system. The microstructural features, tensile properties and stretch flangeabilities of these steels were determined. In order to reveal the fracture mechanism operative during the hole formation and expansion process, the microstructural and damage evolutions in the shear surfaces and sheared edges during hole punching and hole expansion were observed via SEM technology. Also, relations between metallographic features of initial hole internal surfaces, tensile properties or nanohardness difference between soft ferrite and hard constituents with HER results of all fully annealed candidate DP steels were established to explore crucial factors that strongly affect hole expansion behaviors of ultra-high strength DP steels.

2. Experimental procedure

2.1. Materials and processing

A series of lab heats were designed, melted and cast with compositions as listed in Table 1. Fig. 1 shows the schematic illustration of the post-solidification processing, including rough rolling, finish rolling with water spray cooling to a coiling temperature of 677 ºC (labeled by CTH) or 580 ºC (labeled by CTL), the selection of these two coiling temperatures were described and discussed in the earlier works [33], surface grinding, 60% cold rolling and finally annealing simulated by CGL thermal paths. As shown in Fig. 1, cast ingots were hot rolled and cold rolled to the thickness of 1.2 mm. Concerning the intercritical annealing process, two CGL simulations, as seen in Fig. 1, were conducted using the Gleeble 3800. After steel specimens were reheated at +5 ºC s^{-1} to different intercritical annealing temperatures (IATs) according to different aluminum contents and soaked for 60 s, they were separated into two groups. The first group of specimens were fast cooled at −15 ºC s^{-1} to the zinc pot temperature of 460 ºC and held for 15 s, followed by fast cooling to room temperature at −10 ºC s^{-1}. Other steel samples were fast cooled at −15 ºC s^{-1} to a supercooling temperature of 250 ºC (near the M_{90} temperature of the intercritically formed austenite), held for 20 s, up-quenched at +42 ºC s^{-1} to 460 ºC, soaked for 15 s, and then fast cooled to room temperature at −10 ºC s^{-1}. The first intercritical annealing path simulating a standard galvanizing process was designated by GI. The other one was called the supercooling process, designated by SC.

Table 1

The identifications (IDs) and compositions (wt. %) of the candidate DP steels

IDs	C	Al	Cr	Mn	Ni	Si	V	N
DP1	0.15	0.04	0.50	2.00	0.001	0.40	0.06	0.005
DP2	0.15	0.04	0.50	2.00	0.010	0.40	0.12	0.005
DP3	0.15	0.40	0.50	2.00	0.010	0.40	0.06	0.005
DP4	0.15	0.40	0.50	2.00	0.010	0.40	0.12	0.005
DP5	0.15	0.80	0.50	2.00	0.014	0.40	0.06	0.005

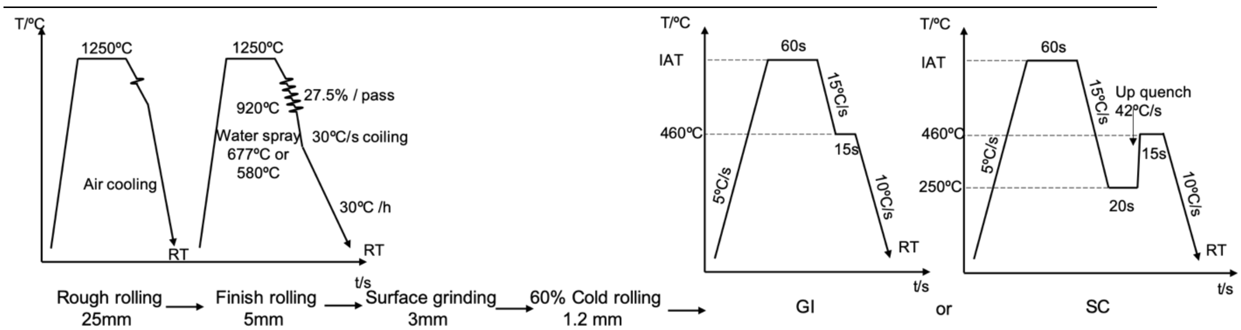

Fig. 1 Schematic illustration of processing

2.2. Materials characterization

Steel specimens were sectioned and cut into small pieces with the dimension of 5 mm × 10 mm × 1.2 mm, using a Buehler Isomet 1000 diamond cutting saw and mounted with Bakelite powder. Then, the mounts were ground with silicon carbide abrasive papers, ranging from 600 to

1200 grit. Next, the specimens were mechanically polished with the 1-μm and 0.3-μm diamond polishing paste to remove the scratches caused by grinding. After that, the samples were polished with the 0.05-μm alumina polishing suspension in a vibrating polisher to eliminate the residual strain caused by mechanical grinding and polishing. Finally, the surface of each mount was etched by 2% Nital reagents to reveal the metallographic features of different phases. A FEI Scios Dual Beam scanning electron microscopy (SEM) was applied to observe the SEM specimens, conducted at the working distance of 10 mm, the accelerating voltage of 20 KeV, and the current of 13 nA. The measurement of retained austenite of all candidate DP steels was conducted by a Lakeshore vibrating sample magnetometer (VSM). The VSM specimens were machined with the dimension of 5 mm in length × 3 mm in width × 1.2 mm in thickness. The VSM specimen of each steel condition was measured via VSM at room temperature, soaked in liquid nitrogen at −40 ºC and measured again. The amount of retained austenite was determined by the comparisons in saturation magnetization of the VSM specimens of the same steel condition with/without austenite.

2.3. Mechanical testing

Tensile testing was performed by a ZwickRoell Z100 material testing machine. The sub-sized tensile specimens with the gauge length of 10 mm were machined following ASTM E8 [34] and oriented transverse (T) to the rolling direction (RD). Two tensile specimens for each steel condition, due to material limitation, were tested and tensile properties (i.e., ultimate tensile strength (UTS), uniform elongation (UE), total elongation (TE) and reduction in area (%RA)) were averaged.

Nanohardness measurements were conducted by a Hysitron TI900 TriboIndenter. A 10 × 10 matrix of nanoindents was performed on the highly polished surface of each steel condition with a Berkovich indenter tip, the load of 2000 μN, and the indent spacing of 7 μm [5]. The nanohardness values were calculated with the application of Oliver–Pharr method [35]. In the wake of nanoindentation testing, the surface of each specimen with indents was slightly etched by 2% Nital reagent and observed via SEM. The nanohardness of specific phase or constituent in each steel condition was determined by averaging all the nanohardness values of indents within the valid regions. For example, regarding ferrite, the valid region is the center of ferrite, excluding the vicinity of ferrite grain boundaries and interfaces between ferrite and hard constituents.

Hole expansion testing was implemented by a BAMPRI hole expansion tester reconditioned and converted from a vintage Tinius Olsen formability tester [36], equipped with new dies, conical punch with the cone angle of 60º and video system, following the requirements of ISO/TS 16630 [37]. Hole expansion specimens were machined with the dimension of 100 mm × 80 mm × 1.2 mm with a 10-mm diameter punched hole in center, conforming to the maximum dimension of CGL simulated samples accommodated by the Gleeble 3800. During hole expansion testing, the initial punched holes were expanded by the conical punch at a constant rate of 30 mm min^{-1}. Each test was stopped, by definition, as the first through-thickness crack was observed. Hole expansion ratio (HER) is calculated by applying Eq. (1) [5,37],

$$HER = \frac{D_f - D_o}{D_o} \times 100\% \quad (1)$$

where, D_o is the initial hole diameter and D_f is the final hole diameter. Additionally, in order to investigate the fracture mechanism of the hole expansion process for ultra-high strength DP steels, partial hole expansion testes were executed and final hole surfaces of hole expansion specimens with different percentages of completion of the hole expansion tests were observed via SEM.

3. Results

3.1. Final microstructures after full CGL Simulations

Fig. 2 shows the final microstructures of the DP steel condition of DP1-CTL after full CGL simulations with GI anneals (Figs. 2 (a) and (b)), and SC anneals (Figs. 2 (c) and (d)). As shown in Fig. 2, GI annealed DP steels were characterized by a mixture of recrystallized ferrite, bainite and fresh martensite. While, the SC annealed DP steels were composed of recrystallized ferrite, bainite, fresh martensite and tempered martensite.

Table 2 summarizes the microstructural features of all fully annealed DP steel conditions. The ferrite grain sizes (d_α) of all steel conditions varied from 2.6 μm to 5.4 μm. It should be noted that lower coiling temperatures led to decreases in recrystallized ferrite grain sizes, as expected. For example, regarding steel conditions of DP3-CTL-GI and DP3-CTH-GI, the change in coiling temperature from 677 ºC to 580 ºC caused a 24% reduction in average ferrite grain diameters from 4.5 μm to 3.4 μm. The volume fractions of fresh martensite ($fv_{(M)}$) for GI annealed DP steels varied between 42.8% to 64.2%. However, the values of fresh $fv_{(M)}$ for the fully annealed DP steels with SC anneals were considerably reduced to 19.0% − 28.7%. Meanwhile, the presence of tempered martensite, ($fv_{(TM)}$) ranged from 21.5% to 43.2%. So, the change in CGL simulations from GI anneals to SC anneals results in a large amount of microstructural replacement of fresh martensite with tempered martensite. The volume percentages of retained austenite of all steel conditions were very small, well below 1% by volume, so the effect of retained austenite on hole expansion behaviors would be negligible.

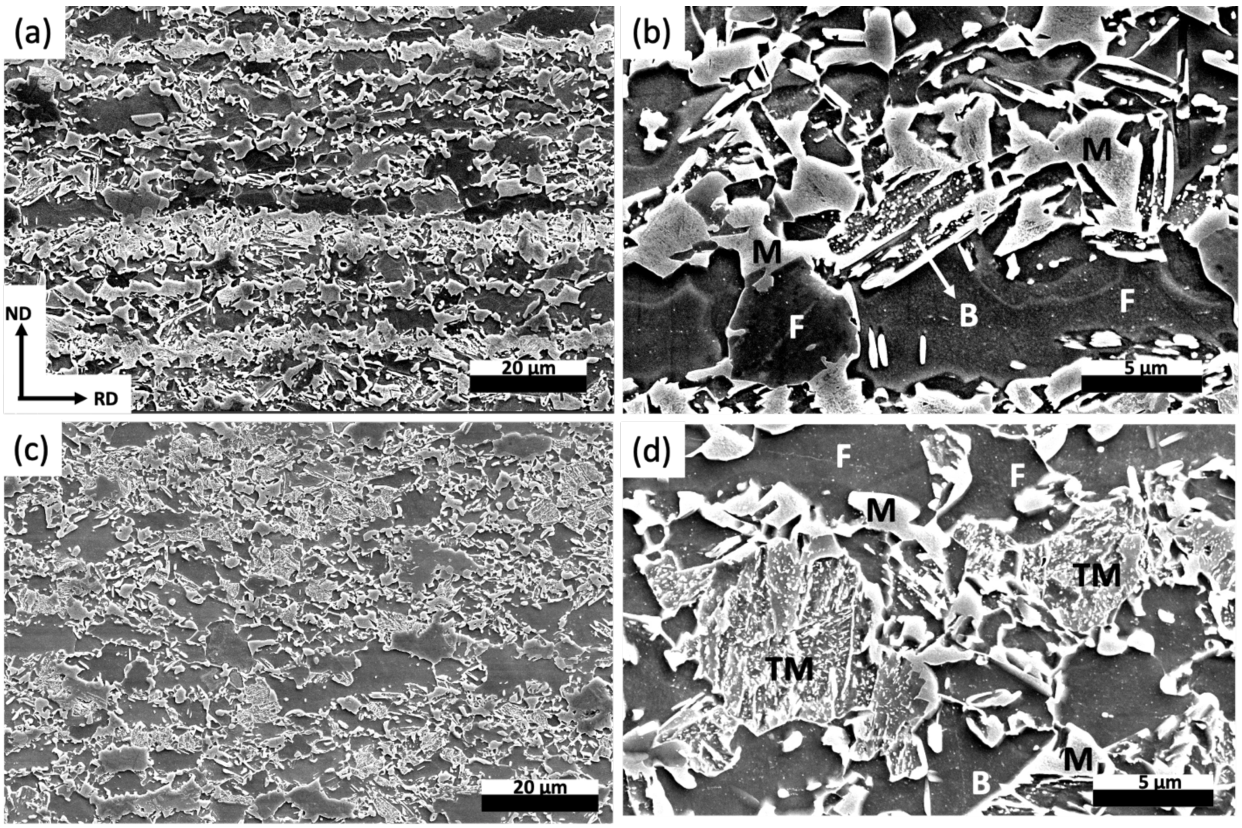

Fig. 2 SEM micrographs of candidate DP steel conditions of (**a**), (**b**) DP1-CTL-GI and (**c**), (**d**) DP1-CTL-SC after full CGL simulations. Ferrite is designated by F, bainite by B, fresh martensite by M and tempered martensite by TM.

Table 2

Microstructural features of candidate DP steels after full CGL simulations, including ferrite grain size (d_F, μm), fresh martensite volume percentage ($fv_{(M)}$, %) and tempered martensite volume fraction ($fv_{(TM)}$, %)

IDs	d_F (μm)	$fv_{(M)}$ (%)	$fv_{(TM)}$ (%)	IDs	d_F (μm)	$fv_{(M)}$ (%)	$fv_{(TM)}$ (%)
DP1-CTL-GI	3.1 ± 1.6	48.8	0	DP1-CTL-SC	3.3 ± 1.7	19.0	43.2
DP2-CTL-GI	2.8 ± 1.3	64.2	0	DP2-CTL-SC	2.6 ± 1.5	23.8	41.6
DP3-CTL-GI	3.4 ± 1.7	50.7	0	DP3-CTL-SC	3.4 ± 1.9	27.5	28.9
DP4-CTL-GI	3.3 ± 1.7	61.8	0	DP4-CTL-SC	3.1 ± 1.6	27.5	37.9
DP5-CTL-GI	5.0 ± 1.9	50.3	0	DP5-CTL-SC	4.7 ± 2.1	28.7	28.6
DP1-CTH-GI	3.7 ± 2.2	42.8	0	DP1-CTH-SC	4.0 ± 2.5	25.6	30.1
DP2-CTH-GI	3.5 ± 2.0	60.8	0	DP2-CTH-SC	3.3 ± 2.1	25.3	34.1
DP3-CTH-GI	4.5 ± 2.4	50.4	0	DP3-CTH-SC	4.3 ± 3.0	26.1	29.2
DP4-CTH-GI	4.0 ± 2.3	48.2	0	DP4-CTH-SC	3.6 ± 1.8	25.9	27.5
DP5-CTH-GI	5.4 ± 2.4	46.3	0	DP5-CTH-SC	5.2 ± 2.3	23.4	21.5

3.2. Microstructural and damage evolutions during hole punching and hole expansion

The complete hole expansion testing consists of hole punching followed by hole expansion. Prior to hold punching, microstructures were fully intercritically annealed and undeformed. After hole punching, the microstructures near the initial hole regions, including initial hole surface (or shear surface) and sheared edge, seen in Fig. 3 (a), were highly deformed. In the wake of hole expansion, the microstructures near the final hole areas were further deformed.

Fig. 3 shows the SEM micrographs of the initial hole internal surface of steel condition DP1-CTL-GI. After hole punching, the initial hole surface was characterized by a rollover zone, a burnished zone, a fracture zone and a shear burr, as observed in Fig. 3 (b). Also, many defects, i.e., micro-voids (Figs. 3 (c) and (d)) and shearing dimples (Fig. 3 (e)), were observed in the initial hole internal surface. These defects may be expected to act as crack initiation sites, and will severely affect the subsequent hole expansion results.

Additionally, Table 3 lists the metallographic characteristics (i.e., area fractions of rollover zone ($fv_{(R)}$), burnished zone ($fv_{(B)}$) and fracture zone ($fv_{(Fx)}$)) of the initial punched hole surfaces of fully annealed DP steel conditions. It is interesting and important to note that the area fractions of the different zones varied with initial processing conditions, and, therefore, initial microstructure. The results of $fv_{(Fx)}$ ranged from 70.2% to 80.0%, accounting for most of the initial hole surfaces. Also, the data of $fv_{(R)}$ and $fv_{(B)}$ varied from 4.5% to 9.2% and 12.7% to 22.2%, respectively.

Fig. 4 displays SEM micrographs of the initial, punched hole sheared edge of candidate DP steel condition of DP1-CTL-GI as viewed in the C (circumference) – Z (thickness) plane. In the wake of hole punching, both ferrite grains and hard constituents (i.e., bainite and fresh martensite) were deformed and elongated along the punching direction with high aspect ratios. In addition, micro-voids or micro-cracks were observed in the shear-affected zone near the burnished-and-fracture transition zone boundary (Fig. 4 (b)), fracture zone boundary (Figs. 4 (c) and (d)), and shear burr boundary (Fig. 4 (e)), which intersected the initial hole surface. These defects predominantly occurred by martensite cracking (Figs. 4 (c) and (e)) and decohesion of the ferrite/hard constituent interfaces (Figs. 4 (b)−(d)). Also, certain tiny micro-voids were found at ferrite/ferrite grain boundaries in the area close to the sheared edge (Fig. 4 (b)).

After hole expansion, with further plasticity, microstructures in the area near the sheared edge were further deformed and elongated along the conical punch displacement lines, seen in Fig. 5. Enhanced strain led to crack growth from the shear-affected zone to the sheared edge, and thus caused edge fracture, as observed in Fig. 5 (c). Also, an irregular edge crack path along with newly nucleated voids nearby resulted from micro-voids nucleation, propagation and coalescence, seen in Fig. 5 (d).

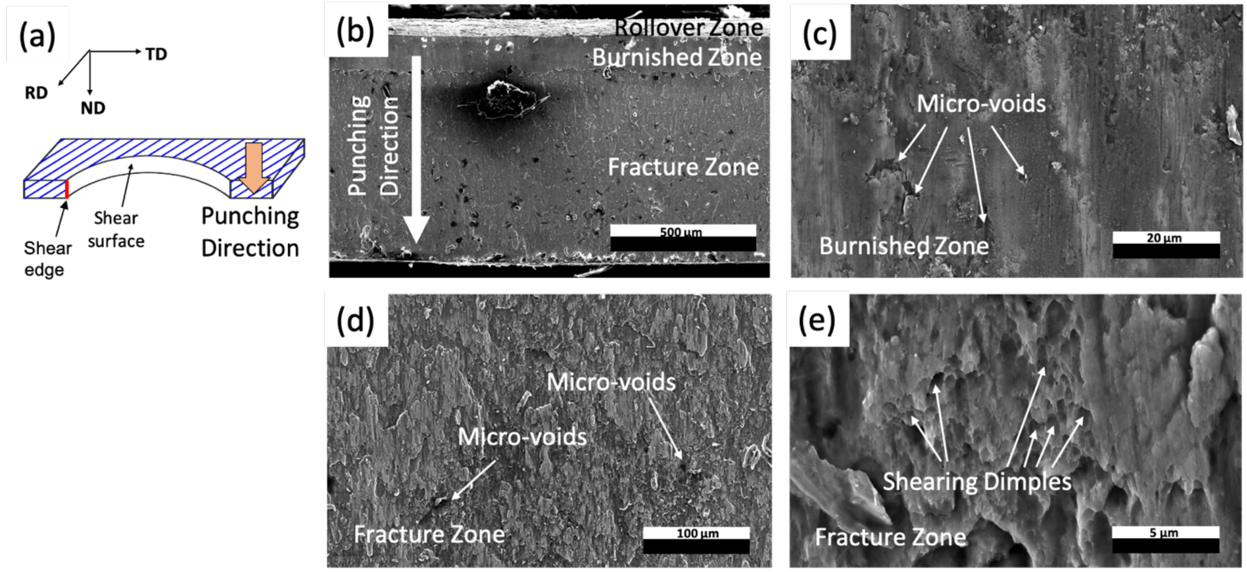

Fig. 3 SEM micrographs of the initial hole surface of candidate DP steel condition of DP1-CTL-GI with (**a**) observation direction of hole expansion specimens, (**b**) overview of through-thickness initial hole surface, and closer observation of (**c**) burnished zone and (**d**), (**e**) fracture zone.

Table 3

The fractions of different zones (rollover zone ($fv_{(R)}$), burnished zone ($fv_{(B)}$) and fracture zone ($fv_{(Fx)}$)) in initial hole surfaces of candidate DP steels after full CGL simulations.

IDs	$fv_{(R)}$ (%)	$fv_{(B)}$ (%)	$fv_{(Fx)}$ (%)	IDs	$fv_{(R)}$ (%)	$fv_{(B)}$ (%)	$fv_{(Fx)}$ (%)
DP1-CTL-GI	6.5	15.3	78.2	DP1-CTL-SC	8.0	21.8	70.2
DP2-CTL-GI	8.5	16.8	74.7	DP2-CTL-SC	7.8	21.9	70.3
DP3-CTL-GI	5.8	14.3	79.9	DP3-CTL-SC	6.7	22.2	71.1
DP4-CTL-GI	8.3	16.2	75.5	DP4-CTL-SC	6.2	19.7	74.0
DP1-CTH-GI	5.9	14.4	79.7	DP1-CTH-SC	4.5	20.9	74.6
DP2-CTH-GI	5.1	15.8	79.1	DP2-CTH-SC	9.2	18.7	72.1
DP3-CTH-GI	7.3	12.7	80.0	DP3-CTH-SC	7.4	19.9	72.7
DP4-CTH-GI	8.4	15.0	76.6	DP4-CTH-SC	9.2	20.1	70.7

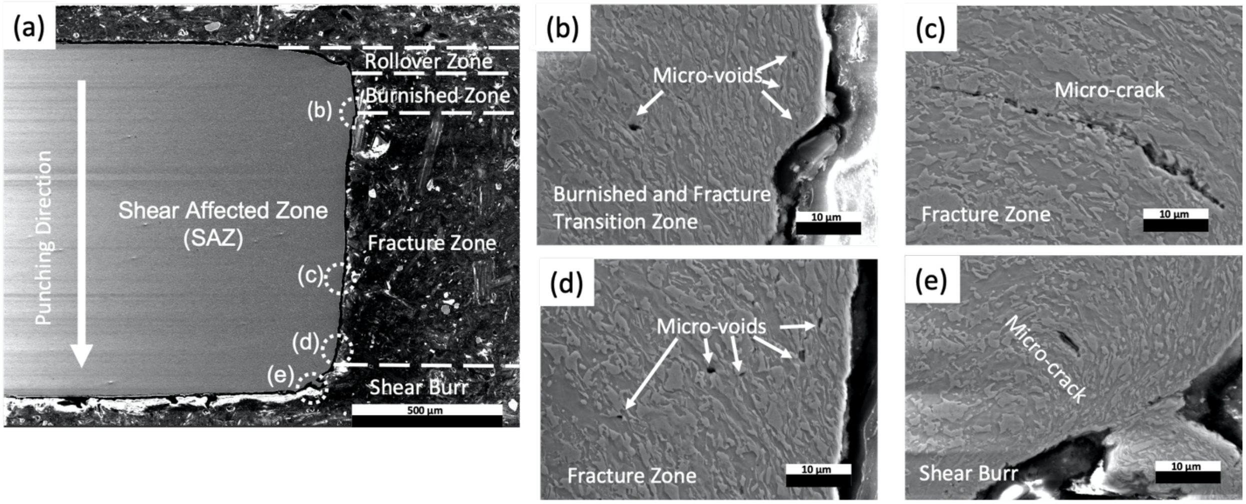

Fig. 4 SEM micrographs of the initial hole sheared edge of candidate DP steel condition of DP1-CTL-GI with (**a**) overview and closer observations of (**b**) burnished-and-fracture transition zone, (**c**), (**d**) transition zone and (**e**) shear burr.

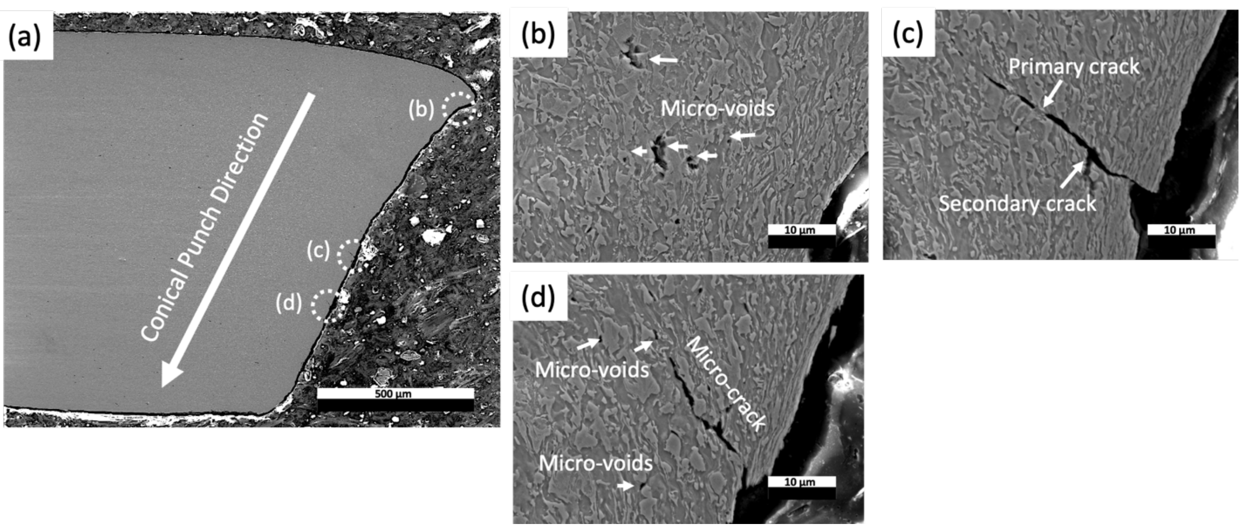

Fig. 5 SEM micrographs of the final hole sheared edge of candidate DP steel condition of DP1-CTL-GI with (**a**) overview and closer observations of (**b**), (**c**) and (**d**) different positions of sheared edge.

In order to investigate the fracture mechanism of the hole expansion process for ultra-high strength DP steels, partial hole expansion tests were performed for one selected steel condition due to material limitation. In this case the punched holes in the selected condition were expanded, with increasing HER values ranging from zero to the final HER value. Fig. 6 shows SEM micrographs of final hole surfaces of steel condition of DP4-CTL-SC in the wake of incomplete hole expansion tests. After hole punching and prior to hole expansion (HER = 0%), micro-voids or micro-cracks introduced by hole punching were observed in both burnished and fracture zones of the initial inner hole surface, Fig. 6 (a). At the early stage of hole expansion (HER = 5%), micro-voids started to grow by void enlargement or micro-cracks began to propagate in the fracture zone, Figs. (b) and (c). As the partial HER increased to 10%, the cracks continued propagating in a zigzagging crack path, indicating ductile fracture, to the upper edge of hole surface and caused a sheared edge crack, Figs. 6 (d) and (e). With further plasticity (HER = 15%), the crack propagated towards the rollover and burnished zones, Figs. 6 (f) and (g). Also, enlarged cracks crossing the shearing dimples can be observed in the fracture zone, Fig. 6 (h). Finally, as the HER value reached to 25%, a through-thickness crack was found in the final hole surface with continuously nucleated micro-cracks or micro-voids, Figs. 6 (i) and (j). At this point the test was discontinued, since the failure criterion had been met.

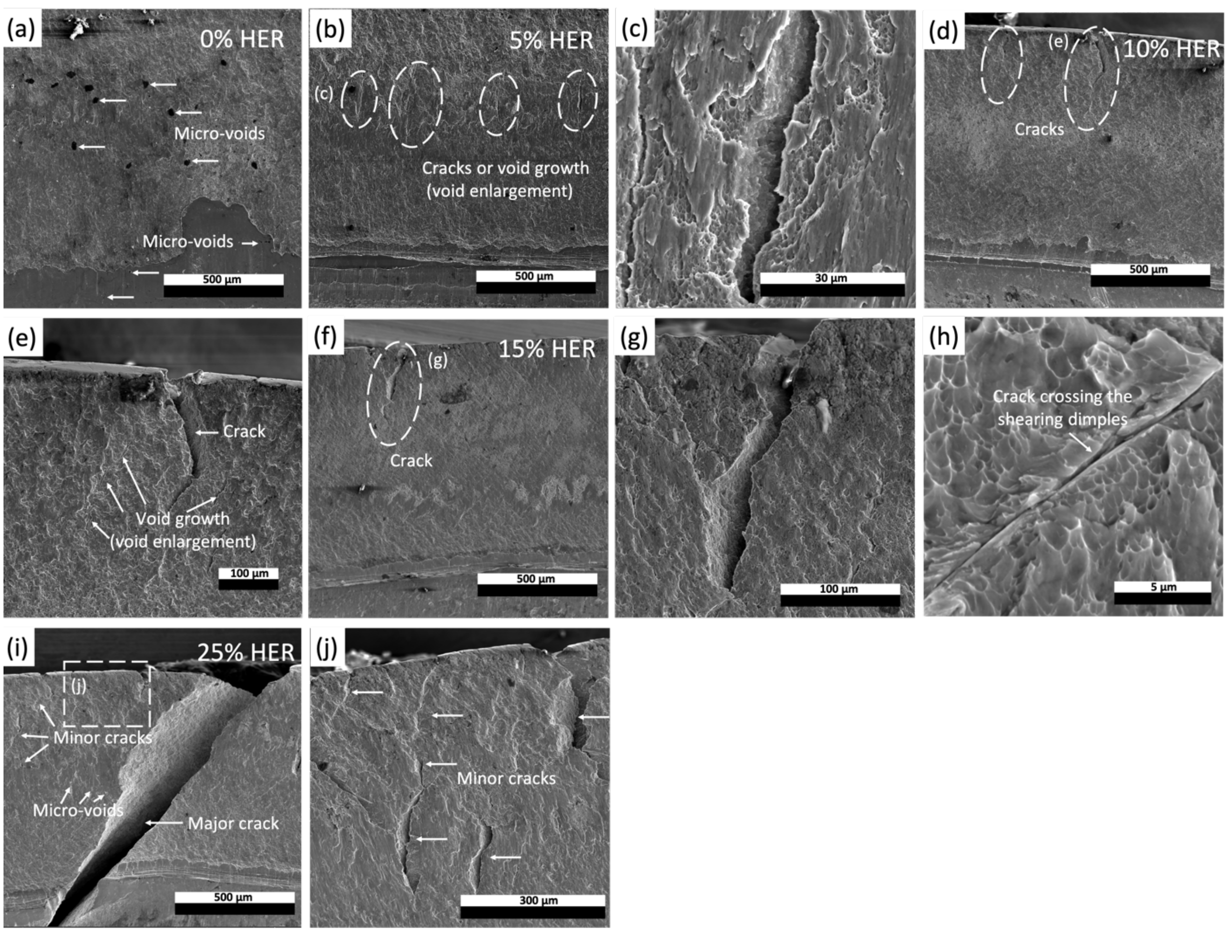

Fig. 6 SEM micrographs of final hole surfaces of candidate DP steel condition of DP4-CTL-SC after different percentages of completion of hole expansion tests.

3.3. Mechanical properties

Tensile properties, including UTS, UE, TE and RA are listed in Table 4. From Table 4, the UTS data of GI annealed and SC annealed DP steels ranged from 1005.9 MPa to 1181.4 MPa and from 936.5 MPa to 1046.0 MPa, respectively. In particular, the steel condition of DP2-CTL-GI (0.04 wt.% aluminum, 0.12 wt.% vanadium, low coiling temperature of 580 ºC and standard galvanizing process) possessed the highest UTS observed in this study of 1181. 4 MPa, which was ascribed to a large amount of fresh martensite and refined ferrite grains with fine VC precipitates, Tables 2 and 4. Also, the steel condition of DP2-CTL-SC had the highest UTS of 1046.0 MPa among all the SC annealed DP steels, Table 4. The combination of a low coiling temperature of 580 ºC and 60% cold reduction led to high stored energy, providing more driving force for ferrite recrystallization and austenite formation during subsequent intercritical annealing, which was discussed earlier in Wu et al.'s work [38]. As mentioned earlier, the loss of UTS was due to the replacement of a large amount of fresh martensite with tempered martensite caused by the change in annealing path from GI anneals to SC anneals.

Table 4

Mechanical properties of candidate DP steels after full CGL simulations

IDs	UTS (MPa)	UE (%)	TE (%)	RA (%)	H_F (GPa)	H_M (GPa)	HER (%)	IDs	UTS (MPa)	UE (%)	TE (%)	RA (%)	H_F (GPa)	H_{TM} (GPa)	HER (%)
DP1-CTL-GI	1092.8	12.3	20.8	27.5	3.1	8.0	17.0	DP1-CTL-SC	974.7	11.9	22.2	36.6	2.6	4.1	27.5
DP2-CTL-GI	1181.4	11.0	19.1	22.6	4.3	9.0	14.5	DP2-CTL-SC	1046.0	10.1	19.0	33.4	2.9	4.4	22.9
DP3-CTL-GI	1086.0	11.6	19.5	29.6	3.3	6.7	17.6	DP3-CTL-SC	973.7	11.7	22.3	29.5	2.4	4.0	26.6
DP4-CTL-GI	1168.2	10.2	17.8	24.6	4.1	9.0	17.0	DP4-CTL-SC	1040.7	10.1	17.6	26.0	3.1	4.8	23.2
DP5-CTL-GI	1061.4	13.4	22.0	25.6	3.3	7.1	19.0	DP5-CTL-SC	983.9	14.1	24.2	33.3	2.7	5.2	21.2
DP1-CTH-GI	1039.1	12.6	17.9	16.6	2.7	7.8	14.6	DP1-CTH-SC	936.5	11.2	19.6	27.1	3.8	4.3	24.3
DP2-CTH-GI	1099.8	11.1	16.2	13.6	3.3	9.2	11.5	DP2-CTH-SC	972.7	10.9	19.2	34.0	2.6	4.4	22.1
DP3-CTH-GI	1059.0	11.0	14.9	24.1	2.4	6.7	17.3	DP3-CTH-SC	950.5	12.0	19.0	26.8	2.8	5.7	22.0
DP4-CTH-GI	1096.9	10.9	16.6	18.5	3.1	8.8	13.2	DP4-CTH-SC	975.9	12.1	20.0	29.4	3.1	4.8	23.5
DP5-CTH-GI	1005.9	14.8	25.3	22.9	2.5	6.7	17.6	DP5-CTH-SC	961.6	15.3	25.0	23.6	2.4	4.8	17.6

Fig. 7 shows the SEM micrographs of steel condition DP1-CTL after full CGL simulations with both GI and SC anneals revealing the nanoindents circuled and highlighted, since a part of indents, especially the nanoindentations performed on hard constituents, were hardly visible after etching. Figs. 7 (b) and (d) present the magnified and selected area of GI and SC DP steel, respectively, illustrating the valid nanoindents or nanohardness values of ferrite and hard constituents (fresh martensite for GI anneals and tempered martensite for SC anneals). Only the indents within the center of phases or constituents were accepted and others were rejected.

The average nanohardness results of ferrite (H_F) and hard constituents (i.e., fresh martensite (H_M) or tempered martensite (H_{TM})) of each steel condition were recorded in Table 4. The data of H_F for all steel conditions ranged from 2.4 GPa to 4.3 GPa. For GI annealed DP steels, the results of H_M ranged from 6.7 GPa to 9.2 GPa. While, in terms of fully annealed DP steel with SC anneals, the values of the hard constituents were remarkably reduced to 4.0 GPa – 5.7 GPa, as a result of the tempering.

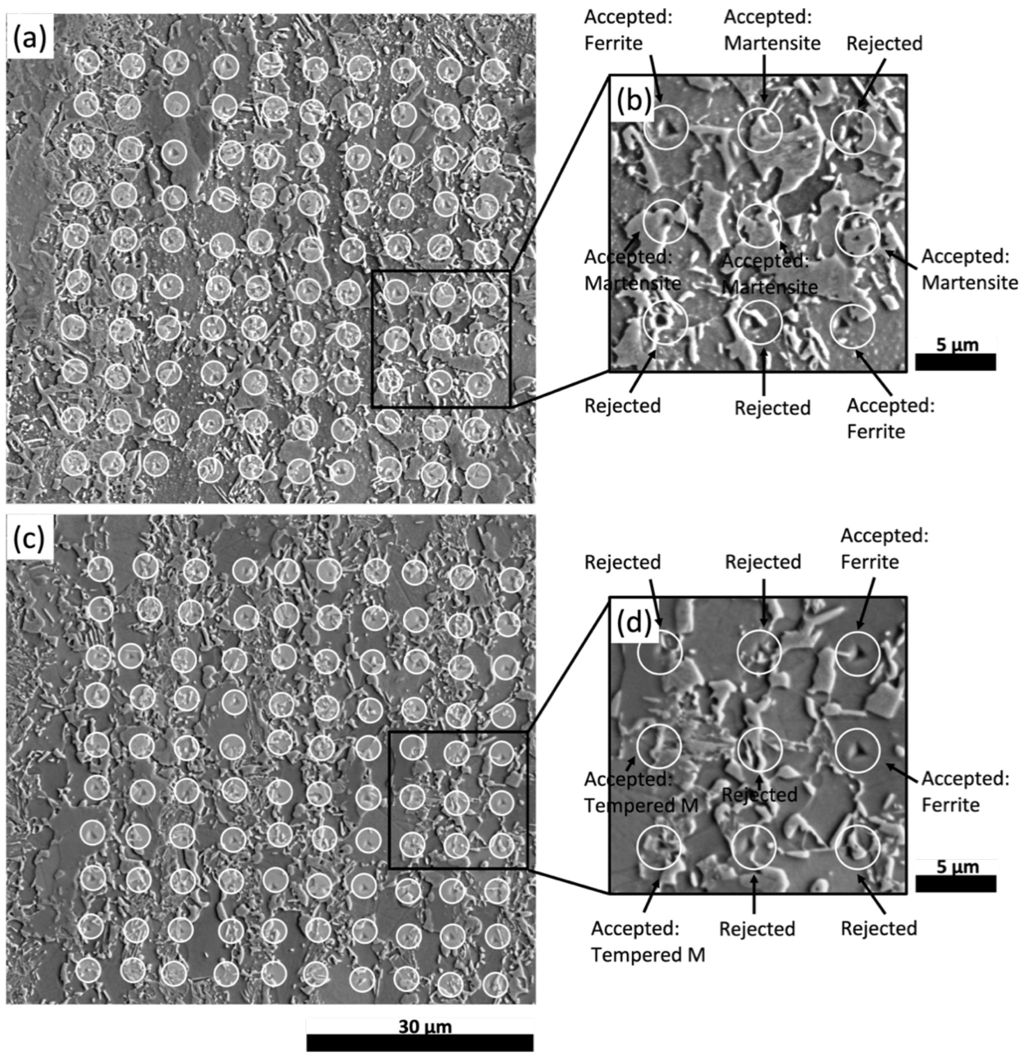

Fig. 7 SEM micrographs of candidate DP steel conditions of (**a**) DP1-CTL-GI and (**c**) DP1-CTL-SC after full CGL simulations with a 10 × 10 matrix of indents, and (**b**) and (**d**) illustrating the magnified and selected area of (**a**) and (**c**), respectively.

The measurements of the HER of GI annealed and SC annealed candidate DP steel conditions ranged from 11.5% to 19.0% and from 17.6% to 27.5%, respectively, also recorded in Table 4. The conspicuous differences in HER values varied with CGL simulations. The change in annealing paths from GI anneals to SC anneals considerably improved hole expansion performances. For instance, the HER value of DP2-CTH-SC was improved by 92.2% from 11.5% and 22.1%, compared with that of DP2-CTH-GI, Table 4.

4. Discussion

The relationships between microstructural features of the initial inner hole surface (i.e., $fv_{(R)}$, $fv_{(B)}$ and $fv_{(Fx)}$) and HER were plotted in Fig. 8. From Fig. 8, the changes in HER values are not relevant to $fv_{(R)}$. However, the HER data increased with increasing $fv_{(B)}$ or reducing $fv_{(Fx)}$, showing that $fv_{(B)}$ and $fv_{(Fx)}$ can be utilized as two critical indicators to evaluate the sheared edge ductility or suggesting a route to improvement. A new index named the burnished to fracture ratio ($fv_{(B)}/fv_{(Fx)}$), which was applied to the assessment for quality of sheared edges in the press shop [39], was also correlated to the results of HER and the plot was shown in Fig. 8. A positive linear relationship between $fv_{(B)}/fv_{(Fx)}$ and HER, can be expressed by Eq. (2), with a coefficient of determination (R^2) of 0.75.

$$HER = 81.19 \times fv_{(B)}/fv_{(Fx)} + 0.15 \tag{2}$$

The vertical and smooth burnished zone is formed, as the punch continued penetrating materials further, in the wake of forming the rollover zone. The formation of the fracture zone starts with the increase in shear stress reaching to a maximum value, at the bottom of the burnished zone, and ends up with the separation of materials. Nakata et al. [40] and Konieczny et al. [41] reported that both $fv_{(B)}$ and $fv_{(Fx)}$ are dependent on UTS, since increasing the values of UTS leads to the reduction in $fv_{(B)}$ or the increase in $fv_{(Fx)}$. Additionally, from the literature [28,39,42,43], $fv_{(B)}$ and $fv_{(Fx)}$ are controlled by cutting clearance. The increase in cutting clearance causes more material to be deformed, resulting in the enlargement of the shear-affected zone (SAZ) and the reduction in the depth of the burnished zone [28,42,43]. In Chintamani et al.'s research [39], $fv_{(Fx)}$ increases as the cutting clearance increases. Thus, from Eq. (2), increasing cutting clearance results in the reduction in $fv_{(B)}/fv_{(Fx)}$ ratio, hence, decreasing the hole expansion behaviors. This is because more micro-voids and shearing dimples are located in the initial hole surface with a higher percentage of rough fracture zone [44], and these defects may act as crack initiation sites, causing crack propagation with further plasticity during hole expansion. Chang et al. [43] investigated the effect of cutting clearance on hole expansion performances of medium-Mn steels and they found smaller cutting clearance contribute to higher HER values. This is due, under smaller cutting clearance, to fewer defects observed near sheared edges and smaller stress or strain concentration regions near sheared edges with less area of deformed microstructures. Additionally, Choi et al.

[45] reported that the height of the shear burr increases with increasing cutting clearance, which is detrimental to hole expansion performances. These indicate that sheared edge ductility is not only influenced by chemical, processing, microstructural characteristics and mechanical properties, but also by the punching operation parameters themselves (i.e., cutting clearance).

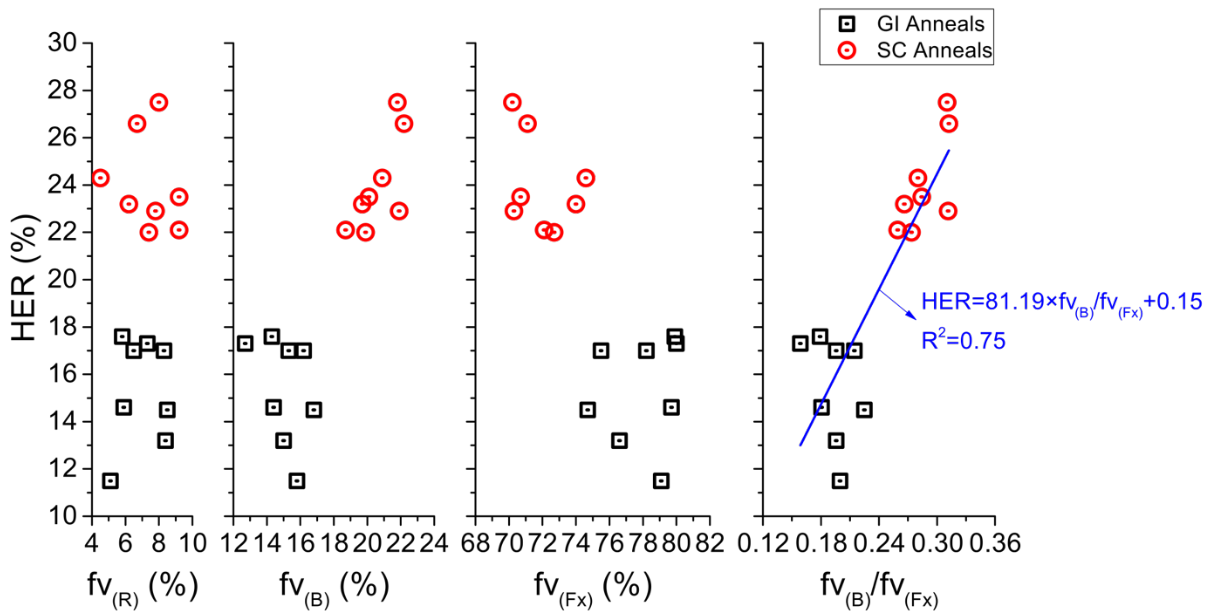

Fig. 8 Correlations of metallographic characteristics of initial hole surfaces and HER values

Since studies of mechanisms of HER or sheared edge ductility are relatively new, obtaining a significant overview is important before studies of detailed micro-mechanisms can be attempted. While the fracture events that terminate the multi-stage deformation, HER tests are ductile in nature, and the HER test results are not controlled by simple ductile fracture in a way similar to a sheet tensile test. It is important to realize that the HER test is in fact the sequence of two deformations: the first caused by punching, nearly pure shear on the Z-theta plane in the Z direction, and the second caused by the hole expansion, i.e., sheet bending followed by balanced biaxial tension, where the plane of biaxial tension is in the sheet plane and normal to the shear direction. The tensile test is quite different in that there is one single deformation passing from yielding through uniform strain to the UTS, triaxial strain from the UTS to the occurrence of the second neck, followed by biaxial strain from the UTS to fracture. Hence, our type of study is very different from those very elegant studies performed by Kahziz et al [30], which consisted of furthering the knowledge base of ductile fracture in simple tension of sheet tensile specimens, or from the tensile deformation of a straight sheared edge, with differences in both geometry and applied strain. In the latter case, it is not clear what the failure criteria are, other than the reduction of ductility properties, as measured in the rolling plane. On the other hand, in a hole expansion test, the failure event has a rather strict definition, i.e., when a crack is found that runs the thickness of the sheet, the test is terminated, and the final hole diameter is measured. It is important to note that at the end of a successful HER test, there is little if any evidence of cracking in the rolling plane even though a crack or cracks can be observed and measured in the sheet thickness direction, even with a length of 1.2 mm or the sheet thickness.

Fig. 9 schematically illustrates the fracture process that occurs during the hole expansion testing. Fig. 9 (a) shows the initial hole surface in the wake of hole punching. Micro-voids or micro-cracks were observed in the burnished zone (Fig. 3 (c)) and fracture zone (Fig. 3 (d)) of the initial hole internal surface. Concerning the damages caused by punching located at the sheared edge and shear-affected zone (SAZ), micro-voids or micro-cracks nucleation were associated with martensite cracking (Figs. 4 (c) and (e)) and debonding at ferrite/martensite interfaces (Figs. 4 (b)-(d)), which is in agreement with the literature [23,27,29,31,46,47]. As the plastic strain increases, these defects acted as crack initiation sites. Micro-cracks started to propagate, and micro-voids began to grow by void enlargement. Also, some of cracks propagated to the upper side of the shear surface, causing a sheared edge crack. With further increasing plastic strain, the crack propagated towards the rollover and burnished zones, with continuously nucleated micro-voids or micro-cracks. When a through-thickness crack was observed in the shear surface, the hole expansion testing was stopped, by definition.

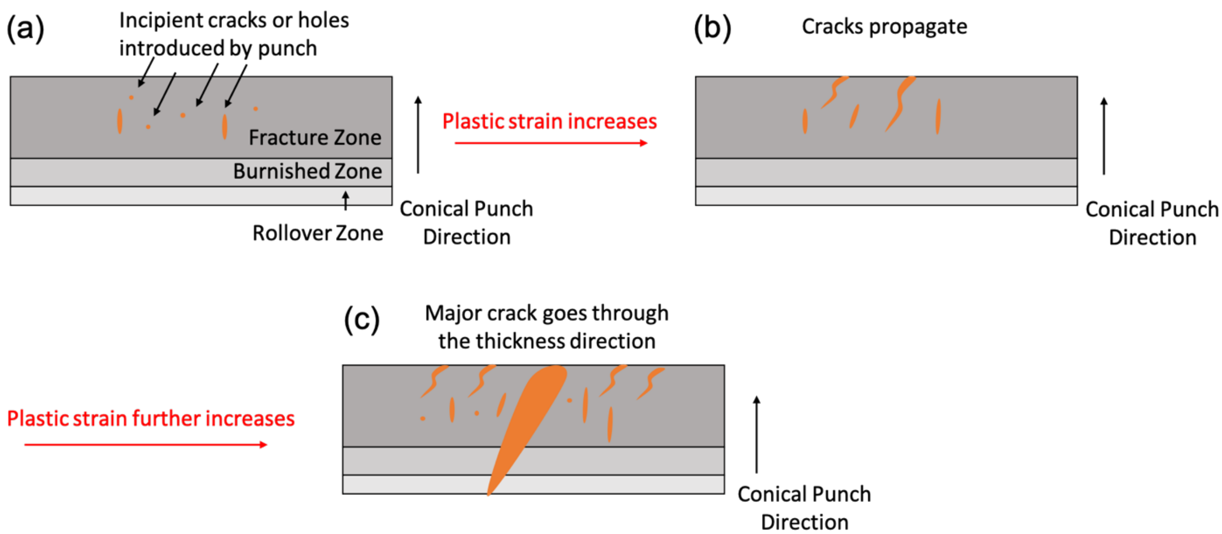

Fig. 9 Schematic illustration of fracture process during hole expansion testing

Fig. 10 presents relations of tensile properties (i.e., UTS, UE, post uniform elongation (Post UE), TE and RA) and HER values from Table 4. However, a general trend for UTS, UE, Post UE or TE with HER was not observed in Fig. 10, which is in contrast to some previous works [10,11,13,14]. This indicates that those general trends obtained from previous studies are only appropriate for monolithic-phase steels and mild steels, and are not necessarily valid for complex-phase steels or advanced high strength steels. However, a reasonable correlation of RA and HER was observed in Fig. 10 (e). This correlation can be expressed by Eq. (3), with a coefficient of determination (R^2) of 0.82.

$$\mathrm{HER} = 0.67 \times \mathrm{RA} + 1.66 \tag{3}$$

The data of RA were determined by the cross-section area difference between initial tensile specimen and the same specimen at the fracture point after fracture. The results of HER were measured by the inner hole diameter difference between original hole expansion specimen and the same specimen with first through-thickness crack observed in the hole surface. During uniaxial tensile testing, the tensile specimens were uniformly deformed prior to necking. Concerning necking, diffuse necking was observed first, followed by localized necking. Paul [48] applied digital image correlation (DIC) technology to measuring local strains at the necked region of tensile specimens and he found that during post uniform deformation, the maximum diffuse strains, at which localized necking initiated, were fairly close to the HER values of the hole expansion specimens with the same materials. According to Fig. 5 (a), extensive uniform thinning was present in the specimen at the point of final fracture. Additionally, during hole expansion testing, strain gradients were observed and simulated by several researchers [10,24,27,49,50], and they found that plastic strains vary with the distance from sheared edges. The amount of strain decreases with increasing distance from the sheared edges. Regarding deformation during the hole expansion process, only localized necking occurred in the inner hole surface [48], intersecting the sheared edge, especially for ultra-high strength DP steels. So, the necking phenomena occurring during both uniaxial tensile testing and hole expansion testing might explain the good correction between RA and HER.

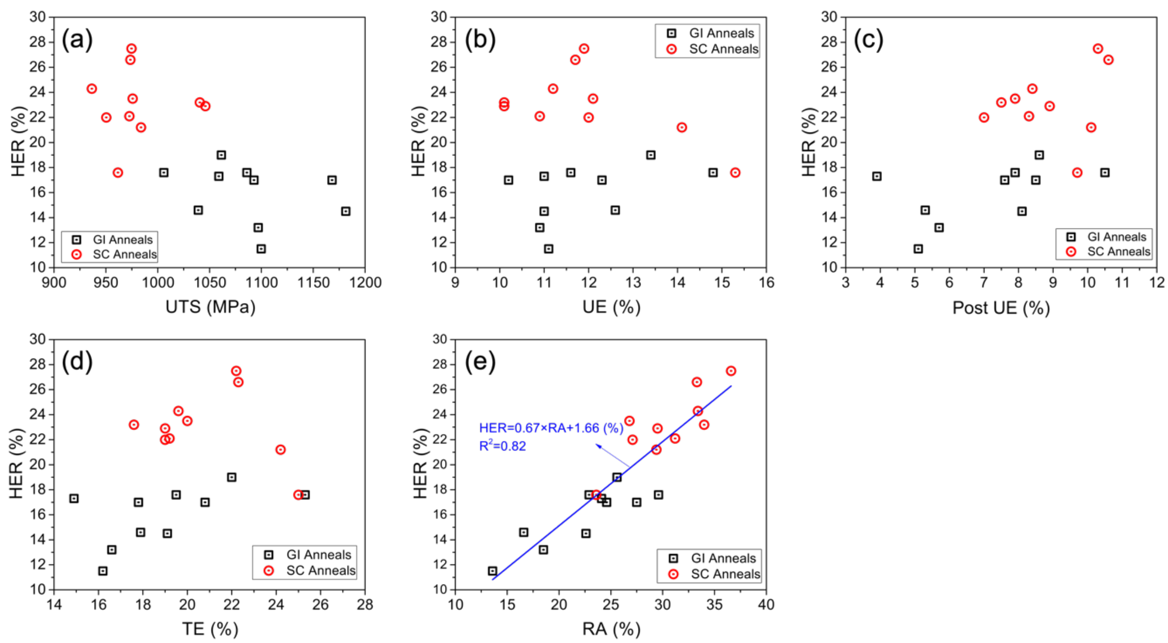

Fig. 10 Correlations of tensile properties and HER results: (**a**) UTS vs HER, (**b**) UE vs HER, (**c**) Post UE vs HER, (**d**) TE vs HER and (**e**) RA vs HER.

Fig. 11 correlated nanohardness difference (H_{diff}) between soft ferrite (H_F) and hard constituents (fresh martensite (H_M) for GI anneals and tempered martensite (H_{TM}) for SC anneals) with HER results in Table 4. This correlation can be given by Eq. (4) with a coefficient of determination (R^2) of 0.78.

$$HER = - 2.4 \times H_{diff} + 27.0 \quad (4)$$

This correlation indicates that HER increases as H_{diff} between ferrite and hard constituents decreases.

The process of producing DP steels, especially the transformation from intercritically formed austenite to fresh martensite, introduces a high dislocation density or more sub-grain structures within both the ferrite and the martensite, and more internal plastic stresses will be expected at ferrite/martensite interfaces or within martensite themself during plastic deformation. Micro-voids or micro-cracks are more likely to be observed associated with debonding of ferrite/martensite interfaces and martensite cracking even at small strains. However, this problem can be resolved by tempering. In current research, tempering fresh martensite resulted in the change in nanohardness data from fresh martensite to tempered martensite, which is ascribed to the reduction in solid solution strengthening due to the formation of cementite and the reduction in dislocation density within martensite [51]. Jardim et al. [52] observed that dual-phase structures with a higher H_{diff} between ferrite and martensite may have a higher possibility of micro-voids nucleation, growth and coalescence associated with decohesion of ferrite/martensite interfaces even at lower strains. In Rosenberg et al.'s investigation [53], a higher degree of strain localization could occur in the low carbon DP steels with a higher H_{diff} between ferrite and hard constituents. Azuma et al. [51] reported that tempering of fresh martensite can increase the critical strain for void nucleation within martensite, which is also beneficial to both global ductility and local ductility of DP steels. Wu et al. [5] reported that a higher strain partitioning to the soft ferrite at the initial hole sheared edge, after hole punching, can be observed for the high strength DP steels characterized by the microstructures with a higher H_{diff}. In the previous study [5], the goal of reducing H_{diff} between soft ferrite and the hard constituents was also achieved via softening fresh martensite by tempering. Before punching, H_F, H_M and H_{diff} between ferrite and fresh martensite were 3.1 GPa, 8.0 GPa and 4.9 GPa, respectively, after the GI anneals, and H_F, H_{TM} and H_{diff} between ferrite and tempered martensite were 2.6 GPa, 4.1 GPa and 1.5 GPa, respectively, after the SC anneals. In the wake of hole punching, all the microstructures in the shear edges were deformed in both GI and SC annealed DP steels. H_F, H_M and H_{diff} between deformed ferrite and deformed fresh martensite in the shear edge near the burnished-and-fracture transition zone with the highest plastic strains causing the initiation of fracture during hole punching, were 5.4 GPa, 11.2 GPa and 5.8 GPa, respectively. Concerning the DP steels with a lower initial H_{diff} after SC anneals, H_F, H_{TM} and H_{diff} between deformed ferrite and deformed tempered martensite in the same relative areas were 3.8 GPa, 5.4 GPa and 1.6 GPa, respectively. The effect of hole punching on the microstructures of steels with a higher H_{diff} is more pronounced. For example, the ferrite and fresh martensite were hardened by 74.2% and 40%, respectively, after the hole punching of the steels given the GI anneal. However, the hardness values of the ferrite and tempered martensite found after the punching of the SC annealed sheets were increased by 46.2% and 31.7%, respectively. These findings indicate that strain partitioning might cause more damage to the matrix, severely affecting subsequent hole expansion performances. So, these studies indicate that one method of improving HER via reducing H_{diff} can be achieved by strengthening ferrite and/or softening martensite.

However, the coefficient of determination of this correlation is not high enough to show a very strong linear relation like the one reported in Hasegawa et al.'s study [23], although in their research, the hardness values of ferrite and martensite were calculated by empirical formulas. This is due to the measurements of nanohardness were performed on the undeformed phases and hard constituents only after full CGL simulations in this study. In the wake of hole punching, the pre-strains caused by punching hardened both ferrite and hard constituents, especially those close to the initial hole sheared edges, as shown in this current study. The plastic strains introduced are not uniform; they decrease as the distance from the sheared edge increases [5,54].

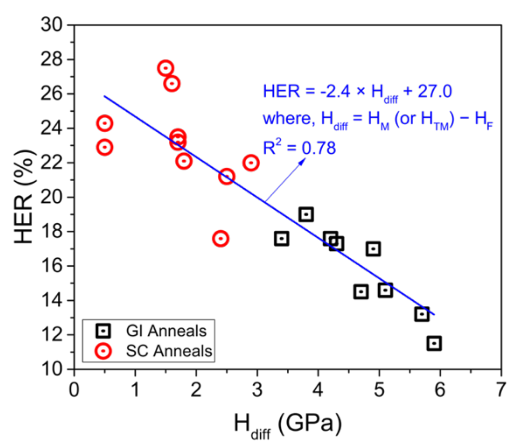

Fig. 11 Correlation of nanohardness difference (H_{diff}) vs HER

5. Conclusions

This paper set out to explore key factors dominating sheared edge ductility of ultra-high strength DP steels. A series of candidate DP steels varying with different pre-annealing conditions and CGL simulations were designed, melted, rolled, annealed and formed. The microstructural and damage evolutions during hole punching and hole expansion were examined via SEM. Correlations of microstructural features of initial hole surfaces, tensile properties and nanohardness difference between ferrite and hardness constituents versus HER results were also constructed. The following findings were concluded.

1. The burnished-to-fracture ratio ($fv_{(B)}/fv_{(Fx)}$) is strongly correlated with hole expansion performance. Since both burnished and fracture zones are influenced by both microstructures and cutting clearance, HER values can be increased by choosing appropriate microstructures and cutting clearance.
2. Hole punching can introduce numerous defects, i.e., micro-voids and micro-cracks. The growth of micro-voids and propagation of micro-cracks result in a through-thickness crack in the shear surface with further plasticity during hole expansion.
3. A good, positive, linear relationship between RA and HER is established, since localized necking occurs during both tensile testing and hole expansion testing with a high degree of strain localization in the ultra-high strength DP steels.
4. The SC annealed DP steels with lower nanohardness differences possess higher HER results, compared with GI annealed DP steels. Hence, the purpose of improving hole expansion behaviors of ultra-high strength DP steels via reducing hardness difference can be achieved by strengthening ferrite and/or softening martensite.

References

[1] N. Fonstein, Advanced high strength sheet steels, 2015. https://doi.org/10.1007/978-3-319-19165-2.
[2] G.R. Speich, V.A. Demarest, R.L. Miller, Formation of austenite during intercritical annealing of dual-phase steels, Metall. Mater. Trans. A. 12 (1981) 1419–1428. https://doi.org/10.1007/BF02643686.
[3] N. Fonstein, H.J. Jun, G. Huang, S. Sriram, B. Yan, Effect of bainite on mechanical properties of multiphase ferrite-bainite-martensite steels, in: Mater. Sci. Technol. Conf. Exhib. 2011, MS&T'11, 2011: pp. 634–641.
[4] Y. Gong, J. Uusitalo, M. Hua, Y. Wu, A.J. DeArdo, Effects of pre-annealing conditions on the microstructure and properties of vanadium-bearing dual-phase steels produced using continuous galvanizing line simulations, J. Mater. Sci. 54 (2019) 7211–7230. https://doi.org/10.1007/s10853-019-03338-6.
[5] Y. Wu, J. Uusitalo, A.J. DeArdo, Investigation of effects of processing on stretch-flangeability of the ultra-high strength, vanadium-bearing dual-phase steels, Mater. Sci. Eng. A. 797 (2020) 140094. https://doi.org/10.1016/j.msea.2020.140094.
[6] R.G. Davies, C.L. Magee, Physical metallurgy of automotive high-strength steels, JOM. 31 (1979) 17–23. https://doi.org/10.1007/BF03354565.

[7] M.S. Rashid, Dual phase steels, Annu. Rev. Mater. Sci. 11 (1981) 245–266. https://doi.org/10.1146/annurev.ms.11.080181.001333.

[8] C.C. Tasan, M. Diehl, D. Yan, M. Bechtold, F. Roters, L. Schemmann, C. Zheng, N. Peranio, D. Ponge, M. Koyama, K. Tsuzaki, D. Raabe, An overview of dual-phase steels: advances in microstructure-oriented processing and micromechanically guided design, Annu. Rev. Mater. Res. 45 (2015) 391–431. https://doi.org/10.1146/annurev-matsci-070214-021103.

[9] J.H. Kim, E.J. Seo, M.H. Kwon, S. Kang, B.C. De Cooman, Effect of quenching temperature on stretch flangeability of a medium Mn steel processed by quenching and partitioning, Mater. Sci. Eng. A. 729 (2018) 276–284. https://doi.org/10.1016/j.msea.2018.05.083.

[10] S.K. Paul, Non-linear correlation between uniaxial tensile properties and shear-edge hole expansion ratio, J. Mater. Eng. Perform. 23 (2014) 3610–3619. https://doi.org/10.1007/s11665-014-1161-y.

[11] O.R. Terrazas, K.O. Findley, C.J. Van Tyne, Influence of martensite morphology on sheared-edge formability of dual-phase steels, ISIJ Int. 57 (2017) 937–944. https://doi.org/10.2355/isijinternational.ISIJINT-2016-602.

[12] X. Fang, Z. Fan, B. Ralph, P. Evans, R. Underhill, The relationships between tensile properties and hole expansion property of C-Mn steels, J. Mater. Sci. 38 (2003) 3877–3882. https://doi.org/10.1023/A:1025913123832.

[13] Y. Gong, M. Hua, J. Uusitalo, A.J. Deardo, Processing factors that influence the microstructure and properties of high-strength dual- phase steels produced using CGL simulations, in: AISTech 2016 Proc., 2016: pp. 2779–2790.

[14] R.J. Comstock, D.K. Scherrer, R.D. Adamczyk, Hole expansion in a variety of sheet steels, J. Mater. Eng. Perform. 15 (2006) 675–683. https://doi.org/10.1361/105994906X150830.

[15] H. Gwon, J.H. Kim, J.-K. Kim, D.-W. Suh, S.-J. Kim, Role of grain size on deformation microstructures and stretch-flangeability of TWIP steel, Mater. Sci. Eng. A. 773 (2020) 138861. https://doi.org/10.1016/j.msea.2019.138861.

[16] J.I. Yoon, J. Jung, H.H. Lee, J.Y. Kim, H.S. Kim, Relationships between stretch-flangeability and microstructure-mechanical properties in ultra-high-strength dual-phase steels, Met. Mater. Int. 25 (2019) 1161–1169. https://doi.org/10.1007/s12540-019-00270-x.

[17] K. Sugimoto, J. Sakaguchi, T. Iida, T. Kashima, Stretch-flangeability of a High-strength TRIP Type Bainitic Sheet Steel., ISIJ Int. 40 (2000) 920–926. https://doi.org/10.2355/isijinternational.40.920.

[18] Y. Gong, The mechanical properties and microstructures of vanadium bearing high strength dual phase steels processed with continuous galvanizing line simulations, University of Pittsburgh, 2015.

[19] B. Mintz, Hot dip galvanising of transformation induced plasticity and other intercritically annealed steels, Int. Mater. Rev. 46 (2001) 169–197. https://doi.org/10.1179/095066001771048754.

[20] H. Matsuda, H. Noro, Y. Nagataki, Y. Hosoya, Effect of retained austenite stability on mechanical properties of 590MPa grade TRIP sheet steels, Mater. Sci. Forum. 638–642 (2010) 3374–3379. https://doi.org/10.4028/www.scientific.net/MSF.638-642.3374.

[21] X. Xu, B.Y. Xu, P. Chen, R.D. Liu, G.D. Wang, H.L. Yi, Effect of austenite stability on the hole expansion behavior of δ-TRIP steels, Mater. Today Commun. 24 (2020) 101034. https://doi.org/10.1016/j.mtcomm.2020.101034.

[22] E. Jimenez-Melero, N.H. van Dijk, L. Zhao, J. Sietsma, S.E. Offerman, J.P. Wright, S. van der Zwaag, The effect of aluminium and phosphorus on the stability of individual austenite grains in TRIP steels, Acta Mater. 57 (2009) 533–543. https://doi.org/10.1016/j.actamat.2008.09.040.

[23] K. Hasegawa, K. Kawamura, T. Urabe, Y. Hosoya, Effects of microstructure on stretch-flange-formability of 980 MPa grade cold-rolled ultra high strength steel sheets, ISIJ Int. 44 (2004) 603–609. https://doi.org/10.2355/isijinternational.44.603.

[24] J.I. Yoon, J. Jung, H.H. Lee, G.-S. Kim, H.S. Kim, Factors governing hole expansion ratio of steel sheets with smooth sheared edge, Met. Mater. Int. 22 (2016) 1009–1014. https://doi.org/10.1007/s12540-016-6346-5.

[25] M.D. Taylor, K.S. Choi, X. Sun, D.K. Matlock, C.E. Packard, L. Xu, F. Barlat, Correlations between nanoindentation hardness and macroscopic mechanical properties in DP980 steels, Mater. Sci. Eng. A. 597 (2014) 431–439. https://doi.org/10.1016/j.msea.2013.12.084.

[26] K. Sugimoto, A. Nagasaka, M. Kobayashi, S. Hashimoto, Effects of retained austenite parameters on warm stretchflangeability in TRlP-aided dual-phase sheet steels., ISIJ Int. 39 (1999) 56–63. https://doi.org/10.2355/isijinternational.39.56.

[27] N. Pathak, C. Butcher, M. Worswick, E. Bellhouse, J. Gao, Damage evolution in complex-phase and dual-

phase steels during edge stretching, Materials (Basel). 10 (2017) 346. https://doi.org/10.3390/ma10040346.
[28] B.S. Levy, C.J. Van Tyne, Review of the shearing process for sheet steels and its effect on sheared-edge stretching, J. Mater. Eng. Perform. 21 (2012) 1205–1213. https://doi.org/10.1007/s11665-011-9997-x.
[29] B.S. Levy, M. Gibbs, C.J. Van Tyne, Failure during sheared edge stretching of dual-phase steels, Metall. Mater. Trans. A. 44 (2013) 3635–3648. https://doi.org/10.1007/s11661-013-1718-7.
[30] M. Kahziz, T.F. Morgeneyer, M. Mazière, L. Helfen, O. Bouaziz, E. Maire, In situ 3D synchrotron laminography assessment of edge fracture in dual-phase steels: quantitative and numerical analysis, Exp. Mech. 56 (2016) 177–195. https://doi.org/10.1007/s11340-015-0076-3.
[31] J.I. Yoon, J. Jung, J.G. Kim, S.S. Sohn, S. Lee, H.S. Kim, Key factors of stretch-flangeability of sheet materials, J. Mater. Sci. 52 (2017) 7808–7823. https://doi.org/10.1007/s10853-017-1012-y.
[32] ASTM E1180-11, Standard test method for measurement of fracture toughness, 2011. https://doi.org/10.1520/E1820-11.2.
[33] Y. Wu, Processing, microstructures and properties of ultra-high strength, low carbon and V-bearing dual-phase steels produced on continuous galvanizing lines, University of Pittsburgh, 2017.
[34] ASTM E8/ E8M-16, Standard test methods for tension testing of metallic materials, ASTM International, Conshohocken, PA, 2016. https://doi.org/10.1520/E0008.
[35] W.C. Oliver, G.M. Pharr, An improved technique for determining hardness and elastic modulus using load and displacement sensing indentation experiments, J. Mater. Res. 7 (1992) 1564–1583. https://doi.org/10.1557/JMR.1992.1564.
[36] P.A. Soloski, N.J. Thimons, A.A. Marks, J. Hartle, Q. Trest, A. Johnston, W. Perisse, A.J. DeArdo, Sheared-edge ductility/hole-expansion ratio testing of advanced high-strength steels, in: Contrib. Pap. from Mater. Sci. Technol. 2015, Columbus, 2015: pp. 917–926.
[37] ISO/TS 16630, Metallic materials-method of hole expanding test, ISO, 2003.
[38] Y. Wu, J. Uusitalo, A.J. DeArdo, Stored energy evaluation for high strength dual-phase steels with different pre-annealing conditions, Metall. Mater. Trans. A. 51 (2020) 4727–4741. https://doi.org/10.1007/s11661-020-05890-2.
[39] J. Chintamani, S. Sriram, Sheared edge characterization of steel products used for closure panel applications, in: SAE Tech. Pap., 2006: pp. 1–8. https://doi.org/10.4271/2006-01-1589.
[40] M. Nakata, K. Uematsu, S. Koseki, Shear deformation properties of ultra high strength steel sheet, in: Int. Deep Draw. Res. Group; Draw. Things to Come; Trends Adv. Sheet Met. Form. ; IDDRG Int. Deep Sheet Met. Form. ; IDDRG, Leca do Balio, Portugal, 2006: pp. 527–534.
[41] A. Konieczny, T. Henderson, On formability limitations in stamping involving sheared edge stretching, SAE Tech. Pap. (2007) 1–12. https://doi.org/10.4271/2007-01-0340.
[42] R. Hambli, S. Richir, Damage mechanics approach in crack growth simulation during the fine blanking process, Int. J. Mater. Prod. Technol. 19 (2003) 466–478. https://doi.org/10.1504/IJMPT.2003.003465.
[43] Y. Chang, S. Han, X. Li, C. Wang, G. Zheng, H. Dong, Effect of shearing clearance on formability of sheared edge of the third-generation automotive medium-Mn steel with metastable austenite, J. Mater. Process. Technol. 259 (2018) 216–227. https://doi.org/10.1016/j.jmatprotec.2018.04.038.
[44] K. Mori, Review of shearing processes of high strength steel sheets, J. Manuf. Mater. Process. 4 (2020) 54. https://doi.org/10.3390/jmmp4020054.
[45] H.-S. Choi, B.-M. Kim, D.-C. Ko, Effect of clearance and inclined angle on sheared edge and tool failure in trimming of DP980 sheet, J. Mech. Sci. Technol. 28 (2014) 2319–2328. https://doi.org/10.1007/s12206-014-0522-7.
[46] T. Okano, C. Inoue, S. Suzuki, K. Yamazaki, S. Toyoda, Reduction of cracks during punching process by cementite in high tensile strength steel sheets, Metall. Mater. Trans. A Phys. Metall. Mater. Sci. 50 (2019) 884–893. https://doi.org/10.1007/s11661-018-5043-z.
[47] T. Sirinakorn, V. Uthaisangsuk, S. Srimanosaowapark, Effects of the tempering temperature on mechanical properties of dual phase steels, J. Met. Mater. Miner. 24 (2014) 13–20. https://doi.org/10.14456/jmmm.2014.3.
[48] S.K. Paul, Fundamental aspect of stretch-flangeability of sheet metals, Proc. Inst. Mech. Eng. Part B J. Eng. Manuf. 233 (2019) 2115–2119. https://doi.org/10.1177/0954405418815370.
[49] N. Pathak, C. Butcher, M. Worswick, Assessment of the Critical Parameters Influencing the Edge Stretchability of Advanced High-Strength Steel Sheet, J. Mater. Eng. Perform. 25 (2016) 4919–4932. https://doi.org/10.1007/s11665-016-2316-9.
[50] L. Chen, J.-K. Kim, S.-K. Kim, G.-S. Kim, K.-G. Chin, B.C. De Cooman, Stretch-flangeability of high Mn TWIP steel, Steel Res. Int. 81 (2010) 552–568. https://doi.org/10.1002/srin.201000044.

[51] M. Azuma, S. Goutianos, N. Hansen, G. Winther, X. Huang, Effect of hardness of martensite and ferrite on void formation in dual phase steel, Mater. Sci. Technol. 28 (2012) 1092–1100. https://doi.org/10.1179/1743284712Y.0000000006.

[52] O.R. Jardim, W.P. Longo, K.K. Chawla, Fracture behavior of a tempered dual phase steel, Metallography. 17 (1984) 123–130. https://doi.org/10.1016/0026-0800(84)90016-8.

[53] G. Rosenberg, I. Sinaiová, Ľ. Juhar, Effect of microstructure on mechanical properties of dual phase steels in the presence of stress concentrators, Mater. Sci. Eng. A. 582 (2013) 347–358. https://doi.org/10.1016/j.msea.2013.06.035.

[54] T. Yokoi, H. Shuto, K. Ikeda, N. Nakada, T. Tsuchiyama, T. Ohmura, Y. Mine, K. Takashima, Quantification of large deformation with punching in dual phase steel and change of its microstructure –Part I: Proposal of the quantification technique of the punching damage of the dual phase steel, ISIJ Int. 56 (2016) 2068–2076. https://doi.org/10.2355/isijinternational.ISIJINT-2016-312.